Title

GABAergic Inhibition Controls Receptive Field Size, Sensitivity, and Contrast Preference of Direction Selective Retinal Ganglion Cells Near the Threshold of Vision

Journal

Journal of Neuroscience, 44(11)

ISSN

0270-6474

Authors

Roy, Suva
Yao, Xiaoyang
Rathinavelu, Jay
et al.

Publication Date

2024-03-13

DOI

10.1523/jneurosci.1979-23.2023

Systems/Circuits

GABAergic Inhibition Controls Receptive Field Size, Sensitivity, and Contrast Preference of Direction Selective Retinal Ganglion Cells Near the Threshold of Vision

Suva Roy,[1]* Xiaoyang Yao,[2]* Jay Rathinavelu,[2] and Greg D. Field[1]

[1]Department of Ophthalmology, Jules Stein Eye Institute, University of California, Los Angeles, California 90095 and [2]Department of Neurobiology, Duke University School of Medicine, Durham, North Carolina 27710

Information about motion is encoded by direction-selective retinal ganglion cells (DSGCs). These cells reliably transmit this information across a broad range of light levels, spanning moonlight to sunlight. Previous work indicates that adaptation to low light levels causes heterogeneous changes to the direction tuning of ON–OFF (oo)DSGCs and suggests that superior-preferring ON–OFF DSGCs (s-DSGCs) are biased toward detecting stimuli rather than precisely signaling direction. Using a large-scale multielectrode array, we measured the absolute sensitivity of ooDSGCs and found that s-DSGCs are 10-fold more sensitive to dim flashes of light than other ooDSGCs. We measured their receptive field (RF) sizes and found that s-DSGCs also have larger receptive fields than other ooDSGCs; however, the size difference does not fully explain the sensitivity difference. Using a conditional knock-out of gap junctions and pharmacological manipulations, we demonstrate that GABA-mediated inhibition contributes to the difference in absolute sensitivity and receptive field size at low light levels, while the connexin36-mediated gap junction coupling plays a minor role. We further show that under scotopic conditions, ooDSGCs exhibit only an ON response, but pharmacologically removing GABA-mediated inhibition unmasks an OFF response. These results reveal that GABAergic inhibition controls and differentially modulates the responses of ooDSGCs under scotopic conditions.

Key words: **adaptation; electrode array; retina**

Significance Statement

Light adaptation and parallel processing are two major functions of the retina. Here, we show that parallel processing is differentially regulated between photopic and scotopic conditions across DSGCs. This differential adaptation alters the absolute sensitivity and receptive field size of s-DSGCs relative to other ooDSGC types. These results point to novel roles for previously identified mechanisms that shape the visual responses of ooDSGCs near the absolute threshold of vision.

Introduction

Detecting motion in the environment while accurately estimating its direction and speed are major functions performed by both vertebrate and invertebrate visual systems (Borst et al., 2010; Mauss et al., 2017; Wei, 2018). In mammals, motion and its direction are computed and recomputed at several stages of visual processing (Barlow et al., 1964; Born and Bradley, 2005; Hillier et al., 2017), illustrating the importance of these signals for vision. Motion information is first extracted in the retina, perhaps as early as bipolar cells (Gaynes et al., 2022; Strauss et al., 2022), which along with starburst amacrine cells shape responses of direction-selective ganglion cells (DSGCs; Euler et al., 2002; Yonehara et al., 2011). A major class of DSGCs, the so-called ON–OFF (oo)DSGCs, produce responses that are tuned to one of four "cardinal" directions: superior, inferior, anterior, or posterior. ooDSGCs also exhibit broad speed tuning and send axons to multiple brain areas including the superior colliculus and lateral geniculate nucleus (Huberman et al., 2009; Dhande and Huberman, 2014; Gauvain and Murphy, 2015). Thus, these neurons likely contribute to a range of behaviors that rely on rapidly processing motion in the environment (Sun et al., 2015; Sabbah et al., 2017).

To reliably signal motion between a moonless night and a sunny day, conditions that spans 12 orders of magnitude in light

Received Oct. 19, 2023; revised Dec. 13, 2023; accepted Dec. 21, 2023.

Author contributions: S.R., X.Y., and G.D.F. designed research; S.R., X.Y., and J.R. performed research; S.R. and X.Y. analyzed data; X.Y. and G.D.F. wrote the paper.

We thank Gautam Awatramani for providing the FACx mice. We thank Jon Cafaro and Kiersten Ruda for commenting on the drafts of this manuscript. The work was supported by the NIH/NEI Grants R01 EY024567 and R01 EY031396 (G.D.F.).

*S.R. and X.Y. contributed equally to this work.

The authors declare no competing financial interests.

Correspondence should be addressed to Greg D. Field at gfield@mednet.ucla.edu.

https://doi.org/10.1523/JNEUROSCI.1979-23.2023

intensity (Rodieck, 1998), the retina must maintain high sensitivity while avoiding saturation. Previous studies show that ooDSGCs change their responses between scotopic (rod-mediated) and photopic (cone-mediated) conditions in two major ways. First, under photopic conditions, ooDSGCs exhibit roughly equal responses to increments and decrements of light. However, under scotopic conditions, they lose their "OFF" response and respond primarily to increments of light (Pearson and Kerschensteiner, 2015). Second, the direction tuning of superior-preferring ooDSGCs (s-DSGCs) becomes broader with decreasing light levels, unlike the other three ooDSGC types that maintain tuning width across light levels (Yao et al., 2018). Differential tuning has been explained as an adaptive strategy that sacrifices some information about the direction in order to improve the ability of the population to detect motion (Yao et al., 2018). This suggests that s-DSGCs may be more sensitive to just-detectable stimuli, predominantly signaling the presence of a stimulus, while the other types predominantly signal the direction of motion.

To test this idea, we presented just-detectable, full-field flashes of light to the ex vivo mouse retina while recording the responses of ooDSGCs using a large-scale multielectrode array (MEA). We found that s-DSGCs are ∼10-fold more sensitive to flashes of light near the absolute visual threshold than the other three ooDSGC types and within a factor of three of the sensitivity of ON-α RGCs, one of the most sensitive RGC types in the mouse retina (Takeshita et al., 2017). One possibility for why s-DSGCs are more sensitive than other ooDSGCs is that they integrate signals over a larger area. We tested this by measuring spatial receptive field (RF) sizes and their dependence on gap junction coupling (among the DSGC types, only s-DSGCs are homotypically coupled). Neither RF size nor gap junction coupling could account for the sensitivity difference. Finally, we tested the role of $GABA_A$-mediated inhibition in tuning response sensitivity. Previous work suggested that (1) s-DSGCs receive different amounts of inhibition than other ooDSGC types under scotopic conditions (Yao et al., 2018) and that (2) inhibition controls the absolute sensitivity of many RGCs (Pan et al., 2016). We found that the application of gabazine reduced the sensitivity difference between ooDSGC types by greatly increasing the sensitivity of inferior, posterior, and anterior-preferring ooDSGCs. We also found that GABAergic inhibition controls the RF sizes of ooDSGCs and suppresses their OFF responses under scotopic conditions. These results reveal novel facets to GABA-mediated inhibition shaping ooDSGC contrast preference, RF size, and absolute sensitivity near the visual threshold. The results also suggest a difference in the functional circuitry providing input to s-DSGCs versus other ooDSGC types under scotopic conditions.

Materials and Methods

Animals. All animals were healthy adults between the ages of 2 months and 1 year and housed in 12 h light/dark cycles, in groups of up to five animals per cage with *ad libitum* access to food and water. Both male and female mice were used in the study. All procedures to maintain and use mice were in accordance with the Duke University Institutional Animal Care and Use Committee. C57BL/6J (RRID: IMSR_JAX:000664) mice were acquired from The Jackson Laboratory. FACx mice were acquired from Dr. Gautam Awatramani at the University of Victoria and have been described previously (Yao et al., 2018).

Recording procedures. Animals were dark-adapted overnight and euthanized by decapitation in the dark using infrared converters. Following euthanasia, the eyes were removed, and a piece of dorsal peripheral retina was isolated and mounted on an array of extracellular microelectrodes (MEA) with ganglion cell side down (Yao et al., 2018). To facilitate the delivery of visual stimuli that drove photoreceptor responses, the dorsal retina was used to measure responses from areas where cone photoreceptors exhibit the highest expression of middle-wavelength sensitive opsin (Applebury et al., 2000; Wang et al., 2011). The MEA consists of 519 electrodes with 30 μm spacing, covering a hexagonal region with 450 μm on each side (Field et al., 2010; Yao et al., 2018). While recording, the retina was perfused with Ames' solution (30°C–32°C) bubbled with 95% O_2 and 5% CO_2, pH 7.4.

Spike sorting and electrical image analysis. Recordings were analyzed offline to identify and sort the spikes of different cells into different clusters (Dabrowski et al., 2004; Field et al., 2007; Yu et al., 2017). Briefly, individual spikes were identified by voltage thresholding on every electrode. The spike waveforms were extracted and clustered using a mixture of Gaussian models in a five-dimensional space determined by principal components analysis. Clusters with >10% contamination in the refractory period or <100 spikes were excluded. Neurons sharing >25% of their spike times in common were considered duplicates, and the copy with the fewer number of spikes was excluded from further analysis.

An electrical image (EI) was calculated by averaging the voltage on each electrode 1 ms preceding and 3 ms following a spike, reflecting the cell's position, extent of dendritic arbor, and axon trajectory relative to the electrode array. The orientation of the dorsal–ventral axis in each recording was determined by the direction axons traveled from each RGC in the EIs (Yao et al., 2018). EIs were also used to track individually recorded neurons across light levels and stimulus conditions (Field et al., 2009; Yao et al., 2018).

Light stimulation. The retina was stimulated with a gamma-corrected OLED micro-display refreshing at 60.35 Hz (SVGA + XL Rev3, eMagin). The stimuli were created in MATLAB (Mathworks), projected through the microscope objective (Nikon, CFI Super Fluor 4×), and focused onto the photoreceptor outer segments. The area covered by the video display was 3.2 mm × 2.4 mm at the retina. The emission spectrum of each channel after the light passes through the optical elements between the display and the retina was measured with a spectrometer (CCS100, Thorlabs). In a subset of experiments where full-field stimuli were used (see below), the retina was stimulated with an LED (peak emission, 490 nm; M490L4, Thorlabs) controlled by an Agilent Function Generator. The area covered by the LED at the retina was a uniform circle, 4 mm in diameter. Photon flux was measured as described before, to calibrate the OLED display and the LED flashes (Yao et al., 2018). Three classes of stimuli were used as follows:

1. Flashing squares: Flashing squares presented on the OLED display were used to measure spatial RFs of DSGCs. A single positive-contrast square was turned on for 1 s and turned off for 1 s at one location and presented pseudo-randomly at different (nonoverlapping) locations over the whole stimulation field. The size of a stimulus square was between 60 μm × 60 μm (each side 0.13 times the side of the hexagonal MEA) and 160 μm × 160 μm (each side 0.36 times the side of the hexagonal MEA). The square had 900% Michelson contrast to elicit robust responses. To accurately estimate RF sizes, we used flashes spanning a larger area to measure s-DSGC RFs and smaller area flashes for the other ooDSGC types (Fig. 2*D*,*E*); this could bias the RF size estimates. As a control, we compared RF sizes across cell types with the same flash sizes and found that estimated RF sizes did not vary significantly between flashed squares that were 60–120 μm on an edge.
2. Drifting gratings: Drifting gratings presented on the OLED display were used to distinguish DSGCs from non-DSGCs using classification methods described previously (Yao et al., 2018). Gratings moved in eight directions with speeds ranging from 24 to 2,400 μm/s, at a spatial period of 960 μm (49.2° visual angle) and at 50% Michelson contrast. Drifting gratings of different directions

and speeds were presented in a pseudorandom order. Each grating was presented for 8 s with 2 s of gray screen between presentations. Each grating was presented 3–4 times, and responses were averaged over presentations. ooDSGCs were distinguished from ON DSGCs based on their speed tuning (Yao et al., 2018).

3. Full-field flashes: Full-field flashes were presented with the LED to measure the absolute sensitivity of DSGCs. Flashes were presented in complete darkness. The flash duration varied between 2 and 8 ms, which together with neutral density filters modulated the mean number of delivered photons. A flash of certain strength was delivered every 3 s for 60 repetitions. Flashes with different strengths were presented in order of lowest to highest strength. The brightest flashes were needed to measure the sensitivity of the least sensitive cells, but these flashes produced some mild adaptation (desensitization) in the most sensitive cells. This required the presentation of the stimuli from dimmest to brightest instead of a fully interleaved design. Responses to full-field flashes were then used in a 2AFC discrimination task and ideal observer analysis (see below) to distinguish "flash" and "no flash" epochs. The "no flash" epochs were obtained by collecting 3 min of spontaneous activity at the beginning of each experiment and dividing these into 60, 3 s trials.

Two-alternative forced-choice analysis. The absolute sensitivity of each DSGC was quantified as the fraction of correctly discriminated trials in which a flash was presented ("flash" trials) from trials during which no stimulus was presented ("no flash" trials). The discrimination was performed using a 2AFC analysis (Dhingra and Smith, 2004; Chichilnisky and Rieke, 2005; Field et al., 2019). The response in each trial was summarized by a vector, which specified the spike count as a function of time (in 20 ms bins). Using a subset of the data at each flash strength, a discriminant was calculated by taking the difference between the mean "flash" trials and the mean of the "no flash" trials. A different discriminant was calculated at each flash strength to optimize the discriminant for response latencies and dynamics that changed across flash strengths. Using a different subset of the data, the dot product between the discriminants was calculated for both a randomly selected "flash" trial and a randomly selected "no flash" trial. The dot product with the larger value was classified as the "flash" trial. This procedure was iterated across all "flash" and "no flash" trials without replacement. Performance was calculated as the fraction of correctly classified trials. This "difference of means" discrimination procedure assumes independent and additive noise with no covariance (Duda et al., 2000) and has been shown previously to work well in flash detection tasks applied to salamander RGCs (Chichilnisky and Rieke, 2005). Assuming, independent and additive Gaussian noise, the relation between discrimination performance (probability correct) and signal-to-noise ratio (SNR) is as follows:

$$P_c = \frac{1}{\sqrt{2\pi}}\int_{-\infty}^{\mathrm{SNR}} e^{-\frac{x^2}{2}}dx \tag{1}$$

$P_c = 0.84$ was set to be the detection threshold because it corresponds to an SNR = 1. Cells with sensitivity curves that never exceed 0.84 were excluded from the analysis.

The discrimination performance curves were fitted to the Naka–Rushton equation as follows: $P_c = 0.5 \times \frac{C^n}{C^n + C_{50}^n} + 0.5$, where C is the flash intensity, C_{50} is the semi-saturation constant, and n is a coefficient proportional to the slope of the sensitivity curve at C_{50}.

Rod photoreceptor simulation and pooling model. A model of rod responses was used to test how differences in RF size across DSGCs impact their predicted thresholds to just-detectable flashes in a 2AFC task (Fig. 3). The simulation and pooling of rod signals were examined by using a recently published model of rod responses (Field et al., 2019). The model includes specific factors to capture the three dominant noise sources in the rod photocurrent: continuous fluctuations in the dark current (a.k.a. continuous noise; Baylor et al., 1980, 1984), discrete noise events in the dark current produced by the thermal activations of rhodopsin, and variability in the amplitude and kinetics of the single-photon response (Baylor et al., 1979; Rieke and Baylor, 1998; Field and Rieke, 2002b). A rod response, $r(t)$ was generated from the following equation:

$$r(t) = \sum_{n=1}^{N}\left(r_\mu(t) + \sum_i w_i c_i(t)\right) + \sum_{d=1}^{N_d}\left(r_\mu(t - t_d) + \sum_j w_j c_j(t - t_d)\right) + \eta(t) \tag{2}$$

Continuous dark noise, $\eta(t)$, was generated by sampling from a Gaussian distribution and filtering in time to match the power spectrum of measured continuous noise (Field et al., 2019). N photon responses in an individual rod were generated by the first term in Equation 2 by sampling from a Poisson distribution with a mean given by the flash strength on a given trial. The mean single-photon response is given by $r_\mu(t)$, and the covariance of the single-photon response is captured by summing over a weighted set, w_i, of eigenvectors, $c_i(t)$, derived from the covariance matrix of the single-photon responses (Field et al., 2019). Finally, discrete noise events caused by the thermal activation of rhodopsin were captured by the second term of Equation 2: N_d. Thermal isomerizations were obtained using the same formulation used for generating the single-photon responses. N_d was determined by sampling from a Poisson distribution with a mean given by the thermal isomerization rate and each isomerization event occurred at random and independent times given by t_d.

In the original formulation of this model (Field et al., 2019), the noise parameters were derived from measurements of the photocurrent from primate rods. We adjusted these parameters to account for the greater amounts of continuous noise and variability in the single-photon response present in mouse rods (both relative to the amplitude of the mean single-photon response). Specifically, the continuous noise was increased by 22% and single-photon response variability was increased by 37.5% (Field and Rieke, 2002a,b). The kinetics of the single-photon response and the shape of the power spectrum of the continuous noise are both similar between mouse and primate rods, so no adjustments were made to these quantities. The thermal rate in mammalian and mouse rods is somewhat uncertain, with the literature allowing for a wide range of values between 0.001 and 0.015 R*/rod/s, so we chose an intermediate value of 0.005 R*/rod/s (Burns et al., 2002; Fu et al., 2008; Yue et al., 2017; Field et al., 2019). Importantly, this model for simulating rod responses reproduces rod detection and temporal sensitivities in a 2AFC task (Field et al., 2019), supporting the application of this model for analyzing the task performance of a pool of rods.

For linear pooling, the optimal linear discriminant was generated from a set of 5,000 simulated single-photon responses (including dark noise) and 5,000 simulated rod responses that contained only dark noise. A linear discriminant, D, was computed as the difference between the means of these two ensembles: μ_{flash} and μ_{null}.

$$D = \mu_{\mathrm{flash}} - \mu_{\mathrm{null}} \tag{3}$$

We then simulated individual rod responses for a pool of P rods by iterating over Equation 2 for given a flash strength, f. The dot product between individual rod responses and the discriminant was computed and summed over all responses to yield an integer value, R_f.

$$R_f = \sum_i^P r_i(t) \cdot D \tag{4}$$

We also simulated individual rod responses for the same size pool of P rods for a flash strength of 0 (the "no flash" or "null" case). Again, the dot product between individual responses and the discriminant was computed and summed over all responses as in Equation 4 to yield an integer value, R_0. If $R_f > R_0$, the trial was scored as correct; if $R_f < R_0$, the trial was scored as incorrect; and if $R_f = R_0$, the trial was randomly scored as correct with 50% probability. This procedure was iterated over 500 trials to calculate the probability correct in the 2AFC task for flash strength f.

For nonlinear pooling, the discriminant and simulated rod responses were generated in the same manner as described for linear pooling. The only difference was that after computing the dot product of a simulated rod response with the discriminant, the result was weighted by the likelihood ratio between the probability that the response arose from the distribution of single-photon responses versus the distribution of continuous noise. These probabilities were estimated by generating two separate response ensembles: a training set of 5,000 simulated single-photon responses and another set of 5,000 responses containing only continuous noise. The dot product of each of these response ensembles with the linear discriminant was computed and were nearly Gaussian. Thus, their means and standard deviation were used to summarize the distributions: μ_A, μ_B, σ_A, and σ_B, where A and B denote the distributions of flash and no flash responses, respectively, after computing their dot products with the discriminant. The optimal (Bayesian) nonlinear weighting was thus calculated as follows:

$$R = \sum_{i}^{P} w_i(r_i(t) \cdot D) \tag{5}$$

where,

$$w_i = \frac{G(r_i(t) \cdot D|\mu_A \ \sigma_A) \ \times \ P(1|f)}{G(r_i(t) \cdot D|\mu_B \ \sigma_B) \ \times P(0|f)} \tag{6}$$

where $G(X|\mu,\sigma)$ is the probability of sampling X from a Gaussian distribution with mean, μ, and standard deviation σ; $P(Y|\lambda)$ is the probability of sampling Y from a Poisson distribution with mean λ; and f in Equation 6 is the flash strength, which acts like a prior in the Bayesian sense.

Responses were simulated for flash strength f and compared to responses of flash strength 0. As with linear pooling, if $R_f > R_0$, the trial was scored as correct; if $R_f < R_0$, the trial was scored as incorrect and if $R_f = R_0$; and the trial was randomly scored as correct with 50% probability.

The simulated rod pool sizes were estimated from the RF sizes of the ooDSGCs as follows: given a Gaussian RF size with a standard deviation of 0.012 mm^2 for ooDSGCs (Fig. 2, excluding s-DSGCs), the equivalent pool size for uniformly weighted rod signals is twice as large (0.024 mm^2; Hemila et al., 1998). The number of rods in this RF is 12,000, given a rod density of 500,000 rods/mm^{-2} in mice (Jeon et al., 1998; Volland et al., 2015). s-DSGCs were taken to be eight times larger: 96,000 rods.

Statistical analysis. Unless otherwise noted, population averages are expressed as mean ± SEM. The number of cells and retinas are indicated in the figure legends; n represents the number of cells used unless indicated otherwise. Each retina came from a different mouse. Student's t test, one-way and two-way ANOVA, and Bonferroni correction were used to compare values under different conditions and between different groups. The differences were considered significant when $p \leq 0.05$.

Results

Superior ooDSGCs are 10-fold more sensitive to detecting dim flashes

In a recent study, we showed that s-DSGCs exhibit broader direction tuning and higher response gain at low light levels (Yao et al., 2018). This suggests that s-DSGCs may be more sensitive to just-detectable stimuli than the other three ooDSGC types under scotopic conditions. To test this, we compared the sensitivity of different types of RGCs under dark-adapted conditions to dim flashes of light. Brief (2–8 ms), full-field flashes were delivered to the mouse retina, ex vivo, while recording the spikes of RGCs over an MEA (Fig. 1*A*). Flashes ranged from strengths that rarely elicited spikes (0.001 R*/rod) to strengths that yielded robust spiking (1 R*/rod). Spike rasters of individual RGCs indicated that s-DSGC responded robustly to weaker flash strengths than the other ooDSGC types (Fig. 1*A*).

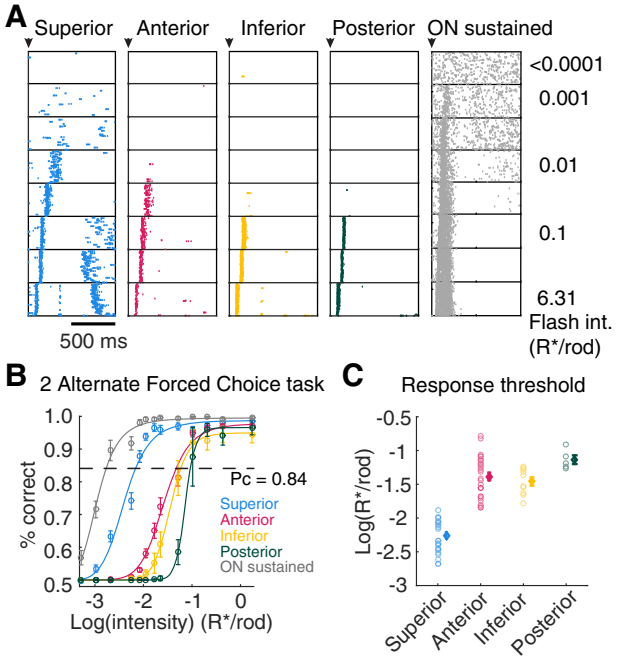

Figure 1. Superior ooDSGCs have a lower absolute detection threshold than other ooDSGCs. ***A***, Rasters show spike responses of example cells to brief, full-field flashes (2–8 ms) in darkness. The top row shows spontaneous activity. The second to bottom rows show responses to flashes with intensity increasing from 0.001 to 6.31 R*/rod. Flashes were presented at the left edge of each panel. For each intensity, flashes were repeatedly delivered every 3 s, 60 times. ***B***, Discrimination performance in a two-alternative forced-choice (2AFC) task, as a function of flash intensity. The dashed line indicates 84% correct in the task (detection threshold). The data were fitted by the Naka–Rushton equation (see Materials and Method). Data were collected from one retina (superior, $n = 16$; anterior, $n = 17$; inferior, $n = 8$; posterior, $n = 5$; ON sustained, $n = 11$). ***C***, Detection threshold of different DSGC types. Each circle shows the detection threshold of an individual cell. Each diamond represents the mean ± SEM threshold of a cell type. ***$p < 0.001$: one-way ANOVA, Bonferroni corrected, between superior and other ooDSGC types. Data from 2 retinas (superior, $n = 31$; anterior, $n = 29$; inferior, $n = 10$; posterior: $n = 5$).

To quantify and compare the sensitivity to dim flashes across RGCs, a two-alternative forced-choice (2AFC) task was performed on spike trains to classify responses as arising from "flash" or "no flash" trials (Chichilnisky and Rieke, 2005). The response classification was based on a linear discriminant learned from training responses and applied to test data (see Materials and Methods). This analysis resulted in a neurometric sensitivity curve (Fig. 1*B*), quantifying the accuracy with which a response predicts the occurrence of a flash over a range of flash intensities. We used the flash intensity that elicited 84% correct in the 2AFC task as the detection threshold; this corresponds to a SNR = 1 (Chichilnisky and Rieke, 2005; see Materials and Methods).

We found that the detection thresholds of s-DSGCs were ~10-fold lower than the other three ooDSGC (Fig. 1*C*, $p < 0.001$), indicating ~10-fold higher sensitivity. Furthermore, the thresholds of the s-DSGCs approached the lowest thresholds observed among any of the recorded RGCs over the MEA (Fig. 1*A*, gray). These were RGCs with sustained ON responses and large spatial RFs (data not shown): these RGCs are likely ON sustained α-cells because they exhibited large spikes over the MEA, presumably produced by large somata (Takeshita et al., 2017; Yu et al., 2017; Ravi et al., 2018). These observations indicated that s-DSGCs are more sensitive to dim flashes of light than the other ooDSGC types and approach (within ~0.5 log unit) the sensitivity of the most sensitive RGCs in the

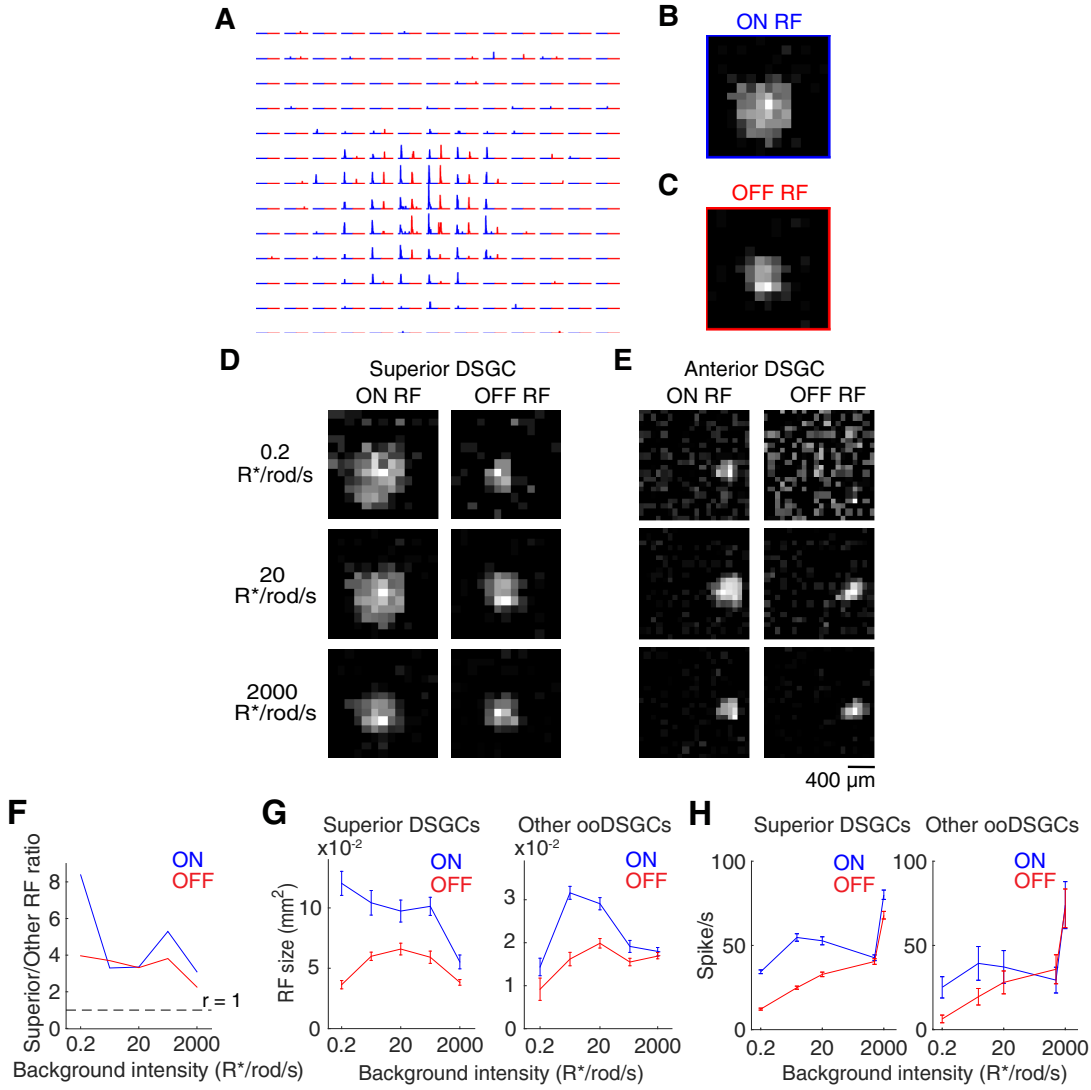

Figure 2. RF sizes of DSGCs depend on the mean light level. ***A***, Spiking response of an example s-DSGC to onset (blue) and offset (red) of flashed squares at each of 169 locations on a 13 × 13 grid. Stimuli were turned on at the beginning of each trace for 1 s and then turned off for 1 s. Data were averaged across five trials for each location. The mean light level was 2,000 R*/rod/s. ***B,C***, ON (***B***) and OFF (***C***) subfields for the cell shown in ***A***. Heat maps calculated from the average spike number at each location normalized to the peak response across the whole field. ***D***, RF of an example s-DSGC across three light levels. Left: ON subfield. Right: OFF subfield. The background light intensity from top to bottom are 0.2, 20, and 2,000 R*/rod/s. The size of the flashing square is 120 µm × 120 µm. ***E***, RF of an example anterior DSGC across three light levels. The size of the flashed square is 80 µm × 80 µm. ***F***, Ratio between s-DSGC and other ooDSGC RF sizes as a function of background light intensity. The dashed line indicates the equal RF size of the two groups. ***G***, Average RF size of DSGCs is plotted as a function of background light intensity. RF sizes were estimated from Gaussian models fitted to heat maps shown in ***B–E***. Left: s-DSGCs ($n = 23$; 2 retinas). Right: combined other three directions ($n = 30$; anterior, $n = 19$; inferior, $n = 6$; posterior, $n = 5$; 2 retinas). One-way ANOVA Bonferroni corrected: $p << 0.001$ for RF size of (i) superior versus other ooDSGCs and (ii) ON versus OFF subfields, for all background intensities <2,000 R*/rod/s. ***H***, Maximum spike rate of s-DSGCs (left) and other ooDSGCs (right) to a square flashed within the RF. The population size of ooDSGC subtypes is the same as in ***G***. The error bars represent SEM.

dark-adapted retina. Below we investigate the mechanisms that produce the higher sensitivity of s-DSGCs than other ooDSGC types under dark-adapted conditions.

Spatial RFs of superior ooDSGCs are larger than other ooDSGC types

One possible explanation for the lower thresholds exhibited by s-DSGCs than the other ooDSGC types is that they have larger RFs, thereby having a larger area in which to collect more photons. To measure the RF size of ooDSGCs, we presented spatially restricted flashes. Each flash was presented at a pseudorandom and nonoverlapping location on the retina; the flash was turned "on" for 1 s with a 1 s interstimulus interval. The 1 s presentation allowed separating ON from OFF responses (Fig. 2*A*, blue and red, respectively) and thus separating the spatial RFs into ON and OFF subfields (Fig. 2*B,C*). The areas of the ON and OFF subfields were then estimated by fitting each with a two-dimensional Gaussian function and computing the area encompassed by the one-sigma contour.

The RF sizes of s-DSGCs were larger than the other three types over a range of light levels spanning scotopic and photopic conditions (Fig. 2*D–G*; $p < 0.001$). The difference was largest at the lowest light level we tested (ON subfield: ratio = 8.4, OFF subfield: ratio = 4.0 at 0.2 R*/rod/s) and smaller at higher light levels (ON subfield: ratio ≃ 3.1, OFF subfield: ratio ≃ 2.3 at 2,000 R*/rod/s). Among the other three types of DSGCs, there was no statistically significant difference in their mean RF sizes at most light levels ($p = 0.063$, one-way ANOVA Bonferroni

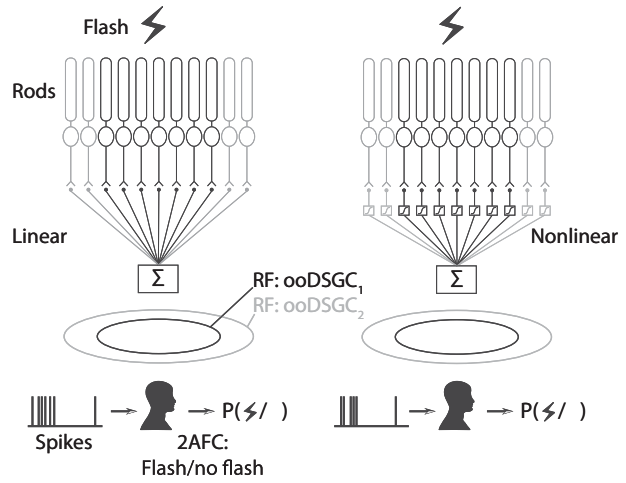

Figure 3. Schematic of the rod pooling model. Dim flash-evoked rod signals under scotopic conditions are pooled by downstream circuits and eventually by ooDSGCs to generate spikes. The pool size of rods is calculated by the size of the RF estimated from flashing square stimulus and density of rods (500,000 rods/mm^2). Black and gray represent cases where different numbers of rods are pooled by ooDSGCs with different RF size. The response across trials is used to predict the presence or absence of a flash in the 2AFC task. Left, linear pooling; right, nonlinear pooling.

corrected for pairwise comparisons: anterior–inferior, anterior–posterior, inferior–posterior); thus, we averaged these data together. These data illustrate that s-DSGCs exhibit larger RFs than the other ooDSGCs and that this difference is largest under low scotopic conditions.

RF sizes of ooDSGCs depend on light level and direction preference

Previous studies have indicated a relatively monotonic relationship between the RF center sizes of non-DS RGCs, with larger RFs under scotopic than photopic conditions (Barlow et al., 1957; Muller and Dacheux, 1997; Troy et al., 1999). Therefore, we sought to test whether ooDSGC RF sizes change monotonically with light level.

For s-DSGCs, ON subfields were largest under scotopic conditions and decreased in a relatively monotonic fashion at higher light levels (Fig. 2*G*, left). However, the OFF subfields of s-DSGCs were largest under mesopic conditions (Fig. 2*G*, left). Among the other ooDSGC types, ON subfields were largest under mesopic conditions and smaller under low scotopic and photopic conditions, while OFF subfields did not change much from mesopic to photopic conditions, but were smaller under scotopic conditions (Fig. 2*G*, right). Finally, across all ooDSGC types, ON subfields were larger than OFF subfields at low light levels but were nearly equal under photopic conditions (Fig. 2*G*). Cumulatively, these results suggest that the underlying circuit mechanisms mediating adaptation are nonuniform across ON and OFF subfields and differ between s-DSGC and other ooDSGC types. We note that RF sizes likely depend on stimulus strength, with larger contrast changes potentially eliciting responses that rise above the threshold near the edge of the RF. The small spots of light we used to probe the RF size were 900% contrast above the background illumination, which is likely to drive responses even near the edge of the RF. Furthermore, natural scenes rarely contain contrasts above this value (Mante et al., 2005). Thus, given these high-contrast probe stimuli, we do not think we are underestimating the RF size under contrasts experienced in typical viewing conditions.

Difference in RF size partially accounts for sensitivity difference

Given the ~8-fold larger ON subfields of s-DSGCS than other ooDSGCs at 0.2 R*/rod/s (Fig. 2*F*), we examined the extent to which this size difference could account for the sensitivity difference in the 2AFC task (Fig. 1). Under a simple model that assumes linear pooling of rod responses with independent and additive Gaussian noise (Fig. 3, left), an eightfold increase in the number of rods will produce an eightfold increase in signal and $\sqrt{8}$-fold increase in noise. This results in a $\sqrt{8}$-fold increase in the SNR. Thus, this simple linear pooling model predicts an ~3-fold increase in the 2AFC performance, significantly less than the ~10-fold difference that we observed (Fig. 1).

This simple analysis has two limitations. First, the dominant source of noise in rods, the thermal activation of rhodopsin, is not a noise source with a zero-mean amplitude distribution. This is because these noise events masquerade as photon responses (Yau et al., 1979). Second, several lines of evidence indicate that the retina is *nonlinearly* pooling rod responses (Field and Rieke, 2002a; Berntson et al., 2004). Thus, we also examined a more complex model in which all sources of rod noise were accurately modeled and rod signals were optimally and nonlinearly pooled (Fig. 3, right; Field et al., 2019). For s-DSGCs and other ooDSGCs, we simulated rod responses in pools of 96,000 and 12,000 rods, respectively (see Materials and Methods). We then performed the same 2AFC ideal observer discrimination task on these simulated responses as we performed on DSGC responses. While the overall performance of nonlinear pooling exceeded a linear pooling model, we observed only a 70% increase in performance between pools of 96,000 and 12,000 rods. This is because the thermal activation of rhodopsin is an asymmetric noise source that does not average to zero as more rods are added to the pool. This results in diminishing returns in sensitivity with larger RF sizes.

Finally, if RF size was the only determinant of the sensitivity difference between s-DSGCs and other ooDSGCs, then sub-RF stimulation should elicit on average the same spiking responses in s-DSGCs and other ooDSGCs. To test this idea, we used the location within the RF where the stimulus squares used to map the RFs (Fig. 2) induced the highest response. If the gain of the s-DSGC and other ooDSGC responses were the same per unit area, then the responses to these stimuli should be the same between the two populations. Instead, the spike rate was higher for s-DSGCs than other ooDSGCs for both ON subfield (34.5 ± 1.4 spike/s vs 22.4 ± 5.9 spike/s) and OFF subfield (15.4 ± 1.0 spike/s vs 6.0 ± 2.4 spike/s) at scotopic conditions (Fig. 2*H*). Note these responses were to high-contrast (900%) stimuli, on a dim background (0.2 R*/rod/s) so they are not just-detectable stimuli at absolute threshold. Nevertheless, they suggest that the gain per unit area of responses in s-DSGCs is substantially higher than the other ooDSGCs at low light levels. This lends further support to the conclusion that mechanisms other than RF size are responsible for the higher sensitivity of s-DSGCs.

To summarize, given an ~8-fold difference in RF size, both a linear and an optimal nonlinear pooling model predict <3-fold difference in sensitivity—much less than the ~10-fold observed sensitivity difference. In addition, locally flashed spots indicated that the gain of responses among s-DSGCs was higher than that for the other ooDSGCs.

Absolute sensitivity and RF size are modestly affected by gap junctions

Given that larger RF size under scotopic conditions does not fully explain the lower threshold of s-DSGCs (Figs. 1, 2), we sought to

identify the underlying mechanisms that cause these differences. One of the major differences between s-DSGCs and other ooDSGCs is that s-DSGCs are homotypically coupled with their neighbors via connexin 36–mediated gap junctions: other ooDSGC are not homotypically coupled (Vaney, 1994; Trenholm et al., 2013, 2014). Previous studies have shown that these gap junctions contribute to several properties of s-DSGCs, including broader tuning curves at low light levels (Yao et al., 2018), and priming responses for moving stimuli (Trenholm et al., 2013). To test for a contribution of gap junctions to absolute sensitivity and RF size, we used FACx mice: a conditional knock-out line in which the expression of the connexin36 gene is selectively disrupted in s-DSGCs (Yao et al., 2018). If homotypic coupling plays a significant role in the higher sensitivity of s-DSGCs, then the sensitivity should be reduced (threshold increased) among s-DSGCs in FACx mice. These mice were used instead of the constitutive Cx36 knock-out to avoid disrupting gap junction coupling in the circuits upstream to s-DSGCs, including homotypic coupling among AII amacrine cells and heterotypic coupling between AII amacrine and cone bipolar cells (Bloomfield and Dacheux, 2001).

First, we measured the absolute sensitivity of ooDSGCs in dark-adapted FACx retinas (Fig. 4*A*, see Materials and Methods) and compared it to the sensitivity in WT (C57/BL6-J) retinas (Fig. 4*B*). Similar to WT, s-DSGCs in the FACx retinas exhibit detection thresholds ~10-fold lower than the other three ooDSGC types (Fig. 4*A*). Furthermore, there was no significant difference in the absolute thresholds between WT and FACx retinas for either s-DSGCs ($p = 0.61$) or other ooDSGCs ($p = 0.32$; Fig. 4*B*). Thus, Cx36 gap junctions did not contribute significantly to the higher absolute threshold of s-DSGCs.

Next, we compared the RF size of DSGCs between FACx and WT retinas under scotopic conditions (1 R*/rod/s). Gap junction coupling could potentially increase the RF size of RGCs by pooling photoreceptor signals from a larger area (Shelley et al., 2006). However, we found that the RF sizes of s-DSGCs modestly changed in the FACx retinas relative to WT (Fig. 4*C*,*D*: $p = 0.03$) while the RFs sizes of other ooDSGCs did not change (Fig. 4*C*,*D*: $p = 0.35$, one-way ANOVA, Bonferroni corrected). We also compared ON and OFF subfield sizes between FACx and WT retinas for all ooDSGC types and found no significant difference (data not shown). These results indicate that homotypic gap junction coupling does not produce the difference in absolute sensitivity or RF size between s-DSGCs and other ooDSGCs types. The weak impact of gap junctions on threshold and RF size may be explained by two factors. (1) Gap junction coupling is expected to play a minor role when coupled cells respond to a homogenous full-field stimulus, because the voltage differences among coupled cells will be small. (2) The gap junction conductance in s-DSGCs is small and insufficient to elicit spikelets without coinciding with chemical synaptic input (Bloomfield and Xin, 1997; Trong and Rieke, 2008; Trenholm et al., 2014).

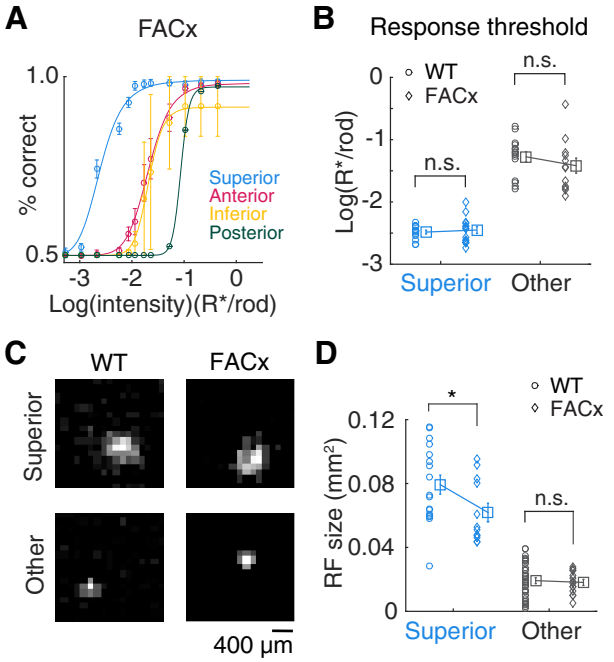

Figure 4. Effect of gap junction coupling on absolute sensitivity and RF size. ***A***, Discrimination performance of DSGCs in FACx mice (one retina; superior, $n = 14$; anterior, $n = 9$; inferior, $n = 2$; posterior, $n = 1$). Data were fitted by the Naka–Rushton equation (see Materials and Methods). ***B***, The detection threshold of different DSGC types in C57 and FACx mice (C57, one retina; s-DSGCs, $n = 14$; other DSGCs, $n = 15$). Discrimination performance curve of individual cells or fitted by the Naka–Rushton equation. Each gray circle or diamond represents the detection threshold of an individual cell. Each presents the mean ± SEM threshold of a cell type. *$p = 0.61$, 0.32 (superior, other); one-way ANOVA, Bonferroni corrected n.s.: not significant. ***C***, Example RFs of s-DSGCs and other DSGCs from C57 and FACx mice. Stimulus square size, 120 µm × 120 µm; background light intensity, 0.2 R*/rod/s. ***D***, Comparison of RF size between s-DSGCs and other DSGCs in C57 and FACx mice (C57s-DSGCs, $n = 17$; FACx s-DSGCs, $n = 12$; C57 other DSGCs, $n = 37$; FACx other DSGCs, $n = 15$). The RF sizes were estimated by summing the ON and OFF responses. Three C57 and two FACx retinas were used in these experiments. *$p = 0.03$, 0.35 (superior, other); one-way ANOVA, Bonferroni corrected.

$GABA_A$ antagonist reduces the sensitivity difference and increases RF size among DSGC types

An alternative mechanism controlling the absolute sensitivity of DSGCs is the effective inhibition that they receive. Previous studies suggest that response thresholds of RGCs fall into distinct groups in mice, with low, medium, and high thresholds (Volgyi et al., 2004). Furthermore, the threshold differences that separate these groups can be mitigated by pharmacologically blocking GABAergic inhibition (Pan et al., 2016). Thus, we hypothesized that the distinction among response thresholds in different ooDSGC types could be caused by differences in effective GABAergic inhibition. To test this possibility, we used the $GABA_A$ receptor antagonist gabazine (SR-95531) to attenuate inhibitory input onto DSGCs and their presynaptic circuits (Yoshida et al., 2001; Pei et al., 2015; see Materials and Methods). The application of gabazine increased the spontaneous firing rate for DSGCs in darkness (Fig. 5*A*), increasing the background noise upon which dim flashes had to be detected. However, our use of a 2AFC task and ideal observer analysis to classify responses as "flash" or "no flash" trials revealed a net increase in the SNR, because detection thresholds were lower following the application of gabazine (Fig. 4*A*–*C*, $p < 0.001$). We observed two key response changes induced by gabazine: (1) absolute sensitivity increased for all DSGCs (Fig. 5*D* dashed lines) and (2) the difference in absolute sensitivity between s-DSGCs and other ooDSGC types decreased from 9.4-fold in control to 3.2-fold in gabazine, on average (Fig. 5*D*, square brackets). We also applied the $GABA_C$ receptor antagonist TPMPA but did not find any further change in the response threshold of DSGCs (data not shown). These results indicate that $GABA_A$ receptor–mediated inhibition largely controls the absolute sensitivity of different types of DSGCs (see Discussion).

We next examined the impact of gabazine on the RF sizes of s-DSGCs and other ooDSGC types. We again measured RF sizes

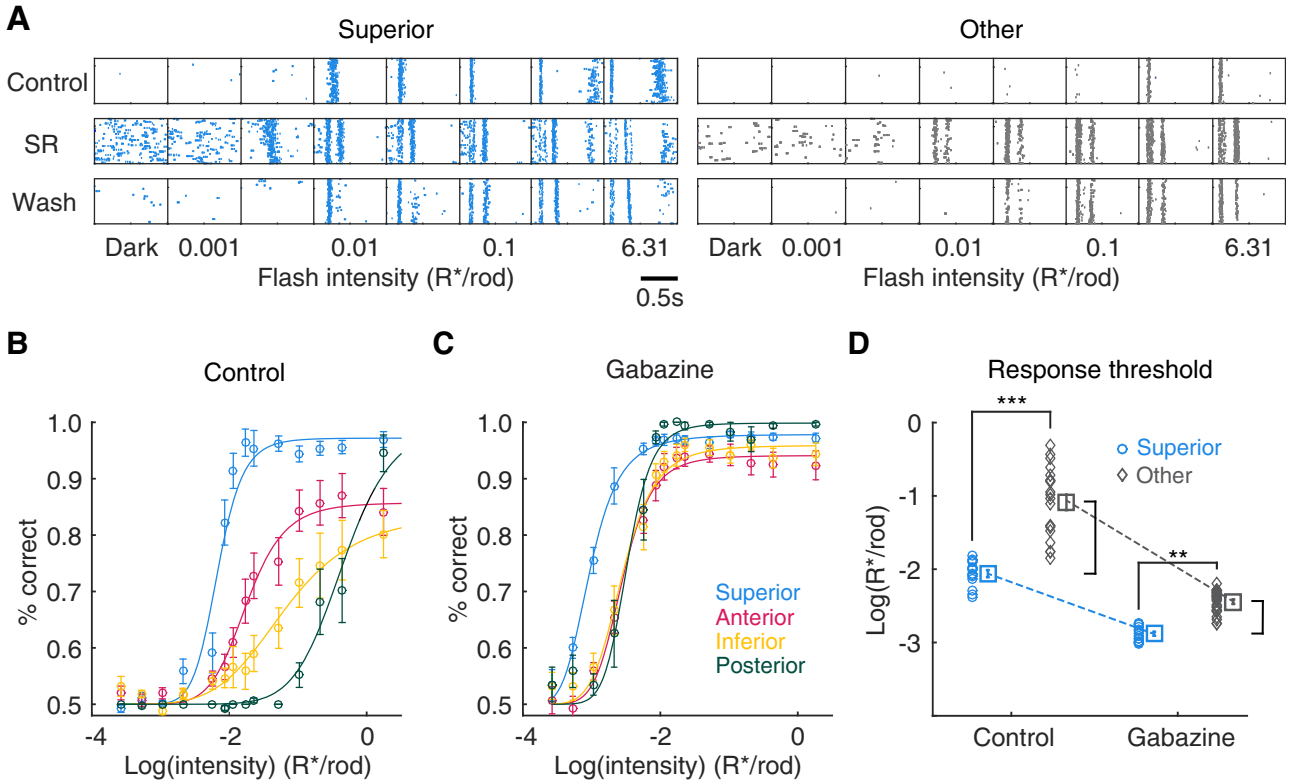

Figure 5. $GABA_A$ blocker decreases the absolute sensitivity of DSGCs. ***A***, Rasters show spike responses of example superior and other ooDSGCs to brief dim full-field flashes (2–8 ms) in darkness under control, gabazine (15 μM), and wash conditions. The leftmost column shows the spontaneous activity of each cell. The second from left to last columns show responses to flashes with intensity increasing from 0.001 to 6.31 R*/rod. Flashes were presented at the left edge of each panel ($t = 0$ s). Flashes were repeatedly delivered every 3 s, 60 repeats. Gabazine was washed in for 5 min and washed out for 30 min. ***B,C***, Discrimination performance of DSGCs from C57BL/6J retinas in control and gabazine conditions (superior, $n = 15$; anterior, $n = 15$; inferior, $n = 10$; posterior, $n = 5$; two retinas). Similar results were observed in a third retina. Data were fitted by the Naka–Rushton equation (see Materials and Method). ***D***, The detection threshold of different DSGC types under control and gabazine conditions. Discrimination performance curves from individual cells were fitted by the Naka–Rushton equation, and the flash strength producing 84% correct (threshold) performance was extracted from the fit. Each circle or diamond represents the detection threshold of an individual cell. Each square represents the mean ± SEM threshold of the population of cells. $^{**}p = 0.003$, $^{***}p < 0.001$, one-way ANOVA, Bonferroni corrected). The dashed lines indicate a decrease in the threshold between superior and non-superior ooDSGCs from control to gabazine conditions. The brackets indicate gabazine-mediated change in sensitivity difference between superior and non-superior ooDSGCs.

of ooDSGCs using 1 s positive-contrast squares, but now with gabazine. The RF areas of all ooDSGC types increased following the application of gabazine (Fig. 6*A,B*). ON subfields exhibited a 40% and 75% increase in area for s-DSGCs and other ooDSGCs, respectively. Surprisingly, there was a much larger fractional increase in RF area for the OFF subfields than the ON subfields under scotopic conditions (Fig. 6*A,B*). OFF subfields exhibited 10-fold and 30-fold increases in the area following the application of gabazine for s-DSGCs and other ooDSGCs, respectively (Fig. 6*B*, right). While the application of gabazine reduced the fractional difference in ON subfield sizes relative to control conditions, s-DSGCs retained RFs that were 1.5-fold larger than the other ooDSGC types (Fig. 6*B*, left).

Previous work has shown that ooDSGCs are typically dominated by OFF responses at high light levels and prefer ON responses at lower light levels (Pearson and Kerschensteiner, 2015). Similarly, our results indicate that the OFF subfields become much smaller than the ON subfields under scotopic conditions (Fig. 2). Application of gabazine increased the OFF subfield size (Fig. 6*B*), and thereby unmasked, under scotopic conditions, a strong OFF response that was similar in amplitude to the ON response (Fig. 6*C*). Together, these results show that in addition to controlling the absolute threshold and RF size of ooDSGCs, GABAergic inhibition also appears to control the contrast preference by masking an OFF response under scotopic conditions.

Discussion

We tested the hypothesis that s-DSGCs are more sensitive than other ooDSGC types near the visual threshold. This hypothesis was based on previous work indicating that s-DSGCs exhibit broader tuning under scotopic conditions and that this broader tuning may be advantageous for detecting motion across the population of ooDSGCs under dimly lit conditions (Yao et al., 2018). We show that the absolute sensitivity of s-DSGCs is ~10-fold greater than that of other ooDSGC types. This difference is largely mediated by differences in effective GABAergic inhibition with a smaller contribution from differences in RF area. We also show that GABAergic inhibition shapes the RF size and effectively masks the OFF responses of ooDSGCs under scotopic conditions. Cumulatively, these results highlight several functional asymmetries across DSGCs, suggesting differences in the circuit mechanisms that produce their responses.

What do these results suggest about DSGC circuits?

The circuit that provides input to DSGCs is perhaps the most intensely studied circuit in the retina. This is largely because

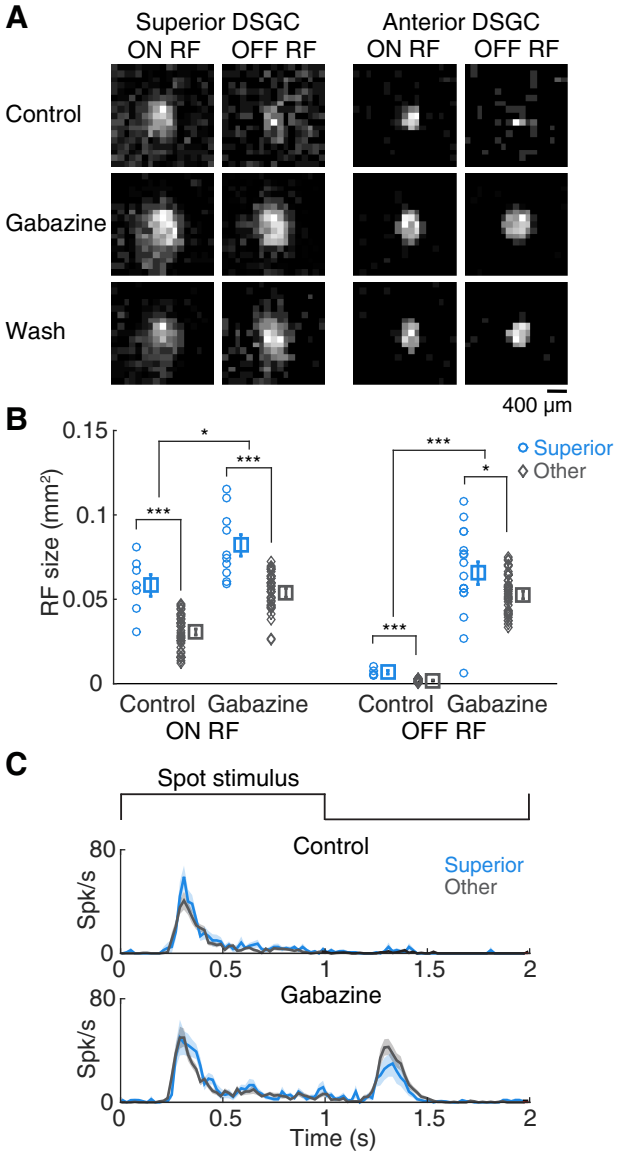

Figure 6. $GABA_A$ blocker increases the RF size of DSGCs. ***A***, RFs of an s-DSGC and anterior-preferring ooDSGC under control and gabazine conditions at a scotopic light level and under wash conditions at a photopic light level. Stimulus was a bright square of size 120 µm × 120 µm at 100% contrast. Background light intensity: 0.2 R*/rod/s, 2,000 R*/rod/s. ***B***, Comparison of RF size across cell types and drug conditions for ON and OFF responses, respectively at 0.2 R*/rod/s (two retinas; superior, $n = 17$; others, $n = 47$). $*p = 0.028$ for control-gabazine ON RF, $*p = 0.012$ for superior-other OFF RF, $***p < 0.001$ (two-way ANOVA, Bonferroni corrected). ***C***, Responses of DSGCs to a single 120 µm × 120 µm bright square stimulus flashing at the center of their receptive fields, under control and gabazine conditions. The center stimulus square was defined as the one that elicited the largest number of spikes for individual ganglion cells (two retinas; superior, $n = 20$; others, $n = 35$). Similar results were observed in a third retina.

the computation performed by the circuit is complex yet precise, requiring finely tuned developmental and synaptic mechanisms (Sethuramanujam et al., 2016, 2017; Ding et al., 2016; Poleg-Polsky and Diamond, 2016a,b; Hanson et al., 2019; Huang et al., 2019). The availability of genetically engineered mouse lines and molecular-genetic approaches also allows manipulating its development and function (Kim et al., 2010; Kay et al., 2011; Chen et al., 2016; Morrie and Feller, 2018). This technical leverage has produced a wealth of knowledge about the cell types that comprise the circuit. Nevertheless, our study provides data that are difficult to explain given previously identified circuit elements. This is probably because relatively few studies have examined changes in ooDSGC physiology from starlight to sunlight and in a manner that distinguishes ooDSGCs based on their direction preference.

Our experimental approach produced two insights. First, s-DSGC (or their excitatory inputs) likely receive less GABAergic inhibition than other ooDSGCs (Fig. 5). This observation predicts that there is a (yet to be identified) GABAergic amacrine cell that is engaged under low scotopic conditions that attenuates the spiking output of inferior-, posterior-, and anterior-preferring DSGCs but minimally attenuates s-DSGC responses (either directly or indirectly; Fig. 7*A*). Second, all ooDSGCs (or their OFF excitatory inputs) receive a source of inhibition that masks OFF responses under scotopic conditions (Fig. 6). This observation predicts yet another GABAergic amacrine cell with selective contacts onto either the outer dendrites of DSGCs and/or onto the OFF bipolar cells that provide input to these dendrites (Fig. 7*B*). These putative amacrine cell types would need to be selectively engaged under scotopic conditions. It is unlikely that this inhibition comes from starburst amacrine cells because (1) we have no evidence that the inhibition is direction tuned, (2) it needs to depend on light level, and (3) the inhibition must be differentially regulated between s-DSGCs and other ooDSGCs.

Finally, we emphasize that these are hypothesized elements of the DSGC circuit that can account for our data. Proving their existence will require intracellular measurements that differentiate pre- versus postsynaptic inhibition and possibly a connectomics approach to identify novel cell types that are synaptically connected to DSGCs or their presynaptic partners (Helmstaedter et al., 2013; Kim et al., 2014; Ding et al., 2016; Bae et al., 2018).

Inhibition limits RGC sensitivity

Different mouse RGC types exhibit distinct absolute sensitivities in darkness, with cells exhibiting threshold responses near one of four flash intensities: ~0.04, ~0.3, ~5, and ~30 R*/rod (Volgyi et al., 2004; Pan et al., 2016). A recent study indicated that inhibition, putatively from amacrine cells, controls the absolute sensitivity of different RGC types (Pan et al., 2016). In particular, they observed that (1) blocking $GABA_C$ receptor–mediated inhibition with TPMPA lowered the absolute threshold of low-sensitive RGCs and (2) blocking $GABA_A$ receptor–mediated inhibition with gabazine lowered the thresholds of a minority of RGCs. It is unclear whether this subset of RGCs were DSGCs, because no moving stimuli were presented (Pan et al., 2016). However, both Pan et al. (2016) and our study indicate that GABAergic inhibition reduces the sensitivity of specific RGC types. In addition, we found that GABAergic inhibition is dominant in the s-DSGCs and weaker but unequal between the three non-superior ooDSGC types (Fig. 5*B*). Thus, many RGC types, including ooDSGCs, receive high-fidelity rod-driven signals that are masked or attenuated by inhibition, suggesting additional differences in presynaptic circuits between these cell types. The purpose of limiting these high-fidelity signals to a minority of RGC types remains unclear. A clue is provided by our previous study, in which DSGCs that retained narrow and relatively high-precision DS tuning were less sensitive to stimuli near visual threshold (Yao et al., 2018). It is possible that RGC types signal complex visual features (e.g., motion direction) instead of acting as photon detectors only when the SNR of visual input is sufficiently high to accurately estimate the feature. Blocking

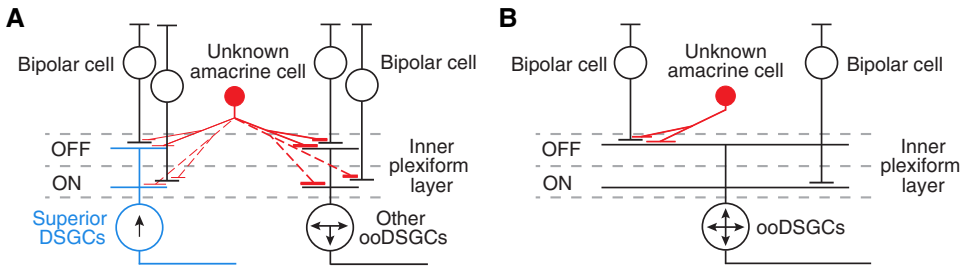

Figure 7. Synaptic organization between putative inhibitory amacrine cells and DSGCs. ***A***, Schematic of possible circuity underlying differential adaptation across DSGCs. Under scotopic conditions, a putative amacrine cell type provides strong (thick red lines) GABAergic inhibition to the other ooDSGCs (or their presynaptic excitatory inputs) and weak (thin red lines) inhibition to s-DSGCs. The solid and dashed lines exemplify mechanisms for OFF and ON RFs respectively. ***B***, Schematic of possible circuit underlying masked OFF responses of ooDSGCs under scotopic conditions. A putative amacrine cell provides GABAergic inhibition to the OFF-layer dendrites of ooDSGCs and/or to the OFF bipolar cells that provide excitatory input to ooDSGCs.

$GABA_A$-mediated inhibition made the thresholds of s-DSGCs and other ooDSGC types more similar, but a clear threshold difference remained (Fig. 5C). While larger RFs of s-DSGCs partially accounted for this residual difference (Fig. 2), our rod pooling model (Fig. 3) suggests that larger RFs only account for ∼50% of the difference. The remainder is likely due to intrinsic differences in the SNR of the s-DSGCs, their synaptic inputs relative to the other ooDSGCs, differential glycinergic inhibition from narrow-field amacrine cells (Jain et al., 2022), and thresholding nonlinearities acting on signals converging at the bipolar cell—RGC synapse (Murphy and Rieke, 2008). Intracellular measurements under dark-adapted conditions are needed to further resolve these differences between the ooDSGC subtypes.

RF size and the influence of light adaptation

Under photopic conditions, we found that s-DSGCs exhibit RFs that are ∼1.5-fold larger than other ooDSGC types (Fig. 2*F*). This means that either s-DSGCs have a higher coverage factor than other ooDSGCs types or they are lower in density. Density estimates of s-DSGCs from the Hb9 mouse line and posterior-preferring ooDSGCs from the DRD4 line indicate ∼80 cells/mm^2 (Trenholm et al., 2011) and 130 cells/mm^2 (Rivlin-Etzion et al., 2011), respectively. This density ratio of 1.6 is similar to our observed RF size ratio of 1.5, suggesting similar coverage factors across ooDSGC types. Thus, DSGCs, like other RGC types appear to sample visual space with similar coverage under photopic conditions (Devries and Baylor, 1997; Gauthier et al., 2009a,b).

The non-monotonic relationship between RF size and light level for DSGCs (Fig. 2*G*) is likely partly shaped by GABAergic inhibition, which appears to reduce RF size below 1 R*/rod/s (Fig. 6). However, measurements of RF size across light levels under both control conditions and with gabazine would require more time and greater stability in the physiology than allowed for in our ex vivo experimental conditions. Thus, we have not fully mapped out the relationship between GABAergic inhibition, RF size, and light level. Another possible mechanism contributing to this non-monotonic relationship is light level dependent changes in homotypic coupling among photoreceptors, horizontal cells, and AII amacrine cells (Bloomfield and Volgyi, 2004; Zhang et al., 2006; Jin and Ribelayga, 2016). Our results suggest that the RF coverage factor across DSGCs is different between scotopic and photopic conditions. Assuming an RF coverage factor of one under photopic conditions, the increase in RF size for s-DSGCs at 0.2 R*/rod/s (Fig. 2) indicates a coverage factor that approaches 3. For the other ooDSGC types at 0.2 R*/rod/s, a slight decrease in RF size suggests that the coverage factor falls below one. Thus, while the RF coverage factor is likely uniform (and ∼1) across RGC types under photopic conditions (Devries and Baylor, 1997; Gauthier et al., 2009a), it appears to vary across RGC types under scotopic conditions.

Role of inhibition in shaping parallel processing

Several recent studies indicate a crucial role for inhibition in differentially shaping parallel processing in the retina. First, inhibition in the outer retina from horizontal cells propagates to the downstream circuit to have diverse influences on RGC function (Drinnenberg et al., 2018). Second, in addition to GABAergic inhibition, glycinergic inhibition strongly modulates BC excitatory signals (Franke et al., 2017). While the effect of glycine on ooDSGC responses may be weaker at scotopic light levels (Pan et al., 2016; Nath et al., 2023), its precise role in shaping RF size and threshold response remains to be investigated. Direction tuning and orientation tuning among RGCs are largely shaped by asymmetric GABAergic inhibition (Barlow and Levick, 1965; Venkataramani and Taylor, 2010; Hanson et al., 2019). This study complements these observations from the perspective of light adaptation. Specifically, adaptational differences across subtypes of DSGCs that control RF size, contrast preference, and absolute sensitivity at low light levels are mediated by GABAergic inhibition. Finally, there have been reports of region-specific differences in the distribution of RGC types across the mouse retina (Zhang et al., 2012; El-Danaf and Huberman, 2019). Since we used the dorsal retina in our studies, it is possible that adaptational effects on DS tuning may be different in other retinal regions (e.g., ventral or nasal), which remains to be discovered.

References

Applebury ML, Antoch MP, Baxter LC, Chun LL, Falk JD, Farhangfar F, Kage K, Krzystolik MG, Lyass LA, Robbins JT (2000) The murine cone photoreceptor: a single cone type expresses both S and M opsins with retinal spatial patterning. Neuron 27:513–523.

Bae JA, et al. (2018) Digital museum of retinal ganglion cells with dense anatomy and physiology. Cell 173:1293–1306.e19.

Barlow HB, Fitzhugh R, Kuffler SW (1957) Change of organization in the receptive fields of the cat's retina during dark adaptation. J Physiol 137:338–354.

Barlow HB, Hill RM, Levick WR (1964) Retinal ganglion cells responding selectively to direction and speed of image motion in the rabbit. J Physiol 173:377–407.

Barlow HB, Levick WR (1965) The mechanism of directionally selective units in rabbit's retina. J Physiol 178:477–504.

Baylor DA, Lamb TD, Yau KW (1979) Responses of retinal rods to single photons. J Physiol 288:613–634.

Baylor DA, Matthews G, Yau KW (1980) Two components of electrical dark noise in toad retinal rod outer segments. J Physiol 309:591–621.

Baylor DA, Nunn BJ, Schnapf JL (1984) The photocurrent, noise and spectral sensitivity of rods of the monkey *Macaca fascicularis*. J Physiol 357:575–607.

Berntson A, Smith RG, Taylor WR (2004) Transmission of single photon signals through a binary synapse in the mammalian retina. Vis Neurosci 21: 693–702.
Bloomfield SA, Dacheux RF (2001) Rod vision: pathways and processing in the mammalian retina. Prog Retin Eye Res 20:351–384.
Bloomfield SA, Volgyi B (2004) Function and plasticity of homologous coupling between AII amacrine cells. Vis Res 44:3297–3306.
Bloomfield SA, Xin D (1997) A comparison of receptive-field and tracer-coupling size of amacrine and ganglion cells in the rabbit retina. Vis Neurosci 14:1153–1165.
Born RT, Bradley DC (2005) Structure and function of visual area MT. Annu Rev Neurosci 28:157–189.
Borst A, Haag J, Reiff DF (2010) Fly motion vision. Annu Rev Neurosci 33: 49–70.
Burns ME, Mendez A, Chen J, Baylor DA (2002) Dynamics of cyclic GMP synthesis in retinal rods. Neuron 36:81–91.
Chen Q, Pei Z, Koren D, Wei W (2016) Stimulus-dependent recruitment of lateral inhibition underlies retinal direction selectivity. eLife 5:e21053.
Chichilnisky EJ, Rieke F (2005) Detection sensitivity and temporal resolution of visual signals near absolute threshold in the salamander retina. J Neurosci 25:318–330.
Dabrowski W, Grybos P, Litke AM (2004) A low noise multichannel integrated circuit for recording neuronal signals using microelectrode arrays. Biosens Bioelectron 19:749–761.
Devries SH, Baylor DA (1997) Mosaic arrangement of ganglion cell receptive fields in rabbit retina. J Neurophysiol 78:2048–2060.
Dhande OS, Huberman AD (2014) Retinal ganglion cell maps in the brain: implications for visual processing. Curr Opin Neurobiol 24:133–142.
Dhingra NK, Smith RG (2004) Spike generator limits efficiency of information transfer in a retinal ganglion cell. J Neurosci 24:2914–2922.
Ding H, Smith RG, Poleg-Polsky A, Diamond JS, Briggman KL (2016) Species-specific wiring for direction selectivity in the mammalian retina. Nature 535:105–110.
Drinnenberg A, Franke F, Morikawa RK, Juttner J, Hillier D, Hantz P, Hierlemann A, Azeredo da Silveira R, Roska B (2018) How diverse retinal functions arise from feedback at the first visual synapse. Neuron 99:117–134.e1.
Duda RO, Hart PE, Stork DG (2000) *Pattern classification*, Ed. 2, New York: Wiley-Interscience.
El-Danaf RN, Huberman AD (2019) Sub-topographic maps for regionally enhanced analysis of visual space in the mouse retina. J Comp Neurol 527:259–269.
Euler T, Detwiler PB, Denk W (2002) Directionally selective calcium signals in dendrites of starburst amacrine cells. Nature 418:845–852.
Field GD, et al. (2010) Functional connectivity in the retina at the resolution of photoreceptors. Nature 467:673–677.
Field GD, Greschner M, Gauthier JL, Rangel C, Shlens J, Sher A, Marshak DW, Litke AM, Chichilnisky EJ (2009) High-sensitivity rod photoreceptor input to the blue-yellow color opponent pathway in macaque retina. Nat Neurosci 12:1159–1164.
Field GD, Rieke F (2002a) Nonlinear signal transfer from mouse rods to bipolar cells and implications for visual sensitivity. Neuron 34:773–785.
Field GD, Rieke F (2002b) Mechanisms regulating variability of the single photon responses of mammalian rod photoreceptors. Neuron 35:733–747.
Field GD, Sher A, Gauthier JL, Greschner M, Shlens J, Litke AM, Chichilnisky EJ (2007) Spatial properties and functional organization of small bistratified ganglion cells in primate retina. J Neurosci 27:13261–13272.
Field GD, Uzzell V, Chichilnisky EJ, Rieke F (2019) Temporal resolution of single-photon responses in primate rod photoreceptors and limits imposed by cellular noise. J Neurophysiol 121:255–268.
Franke K, Berens P, Schubert T, Bethge M, Euler T, Baden T (2017) Inhibition decorrelates visual feature representations in the inner retina. Nature 542: 439–444.
Fu Y, Kefalov V, Luo DG, Xue T, Yau KW (2008) Quantal noise from human red cone pigment. Nat Neurosci 11:565–571.
Gauthier JL, Field GD, Sher A, Shlens J, Greschner M, Litke AM, Chichilnisky EJ (2009a) Uniform signal redundancy of parasol and midget ganglion cells in primate retina. J Neurosci 29:4675–4680.
Gauthier JL, Field GD, Sher A, Greschner M, Shlens J, Litke AM, Chichilnisky EJ (2009b) Receptive fields in primate retina are coordinated to sample visual space more uniformly. PLoS Biol 7:e1000063.
Gauvain G, Murphy GJ (2015) Projection-specific characteristics of retinal input to the brain. J Neurosci 35:6575–6583.
Gaynes JA, Budoff SA, Grybko MJ, Hunt JB, Poleg-Polsky A (2022) Classical center-surround receptive fields facilitate novel object detection in retinal bipolar cells. Nat Commun 13:5575.
Hanson L, Sethuramanujam S, deRosenroll G, Jain V, Awatramani GB (2019) Retinal direction selectivity in the absence of asymmetric starburst amacrine cell responses. eLife 8:e42392.
Helmstaedter M, Briggman KL, Turaga SC, Jain V, Seung HS, Denk W (2013) Connectomic reconstruction of the inner plexiform layer in the mouse retina. Nature 500:168–174.
Hemila S, Lerber T, Donner K (1998) Noise-equivalent and signal-equivalent visual summation of quantal events in space and time. Vis Neurosci 15: 731–742.
Hillier D, et al. (2017) Causal evidence for retina-dependent and -independent visual motion computations in mouse cortex. Nat Neurosci 20:960–968.
Huang X, Rangel M, Briggman KL, Wei W (2019) Neural mechanisms of contextual modulation in the retinal direction selective circuit. Nat Commun 10:2431.
Huberman AD, Wei W, Elstrott J, Stafford BK, Feller MB, Barres BA (2009) Genetic identification of an on-off direction-selective retinal ganglion cell subtype reveals a layer-specific subcortical map of posterior motion. Neuron 62:327–334.
Jain V, et al. (2022) Gain control by sparse, ultra-slow glycinergic synapses. Cell Rep 38:110410.
Jeon CJ, Strettoi E, Masland RH (1998) The major cell populations of the mouse retina. J Neurosci 18:8936–8946.
Jin NG, Ribelayga CP (2016) Direct evidence for daily plasticity of electrical coupling between rod photoreceptors in the mammalian retina. J Neurosci 36:178–184.
Kay JN, De la Huerta I, Kim IJ, Zhang Y, Yamagata M, Chu MW, Meister M, Sanes JR (2011) Retinal ganglion cells with distinct directional preferences differ in molecular identity, structure, and central projections. J Neurosci 31:7753–7762.
Kim JS, et al. (2014) Space-time wiring specificity supports direction selectivity in the retina. Nature 509:331–336.
Kim IJ, Zhang Y, Meister M, Sanes JR (2010) Laminar restriction of retinal ganglion cell dendrites and axons: subtype-specific developmental patterns revealed with transgenic markers. J Neurosci 30:1452–1462.
Mante V, Frazor RA, Bonin V, Geisler WS, Carandini M (2005) Independence of luminance and contrast in natural scenes and in the early visual system. Nat Neurosci 8:1690–1697.
Mauss AS, Vlasits A, Borst A, Feller M (2017) Visual circuits for direction selectivity. Annu Rev Neurosci 40:211–230.
Morrie RD, Feller MB (2018) A dense starburst plexus is critical for generating direction selectivity. Curr Biol 28:1204–1212.e05.
Muller JF, Dacheux RF (1997) Alpha ganglion cells of the rabbit retina lose antagonistic surround responses under dark adaptation. Vis Neurosci 14:395–401.
Murphy GJ, Rieke F (2008) Signals and noise in an inhibitory interneuron diverge to control activity in nearby retinal ganglion cells. Nat Neurosci 11:318–326.
Nath A, Grimes WN, Diamond JS (2023) Layers of inhibitory networks shape receptive field properties of AII amacrine cells. Cell Rep 42:113390.
Pan F, Toychiev A, Zhang Y, Atlasz T, Ramakrishnan H, Roy K, Volgyi B, Akopian A, Bloomfield SA (2016) Inhibitory masking controls the threshold sensitivity of retinal ganglion cells. J Physiol 594:6679–6699.
Pearson JT, Kerschensteiner D (2015) Ambient illumination switches contrast preference of specific retinal processing streams. J Neurophysiol 114:540–550.
Pei Z, Chen Q, Koren D, Giammarinaro B, Acaron Ledesma H, Wei W (2015) Conditional knock-out of vesicular GABA transporter gene from starburst amacrine cells reveals the contributions of multiple synaptic mechanisms underlying direction selectivity in the retina. J Neurosci 35:13219–13232.
Poleg-Polsky A, Diamond JS (2016a) Retinal circuitry balances contrast tuning of excitation and inhibition to enable reliable computation of direction selectivity. J Neurosci 36:5861–5876.
Poleg-Polsky A, Diamond JS (2016b) NMDA receptors multiplicatively scale visual signals and enhance directional motion discrimination in retinal ganglion cells. Neuron 89:1277–1290.
Ravi S, Ahn D, Greschner M, Chichilnisky EJ, Field GD (2018) Pathway-specific asymmetries between ON and OFF visual signals. J Neurosci 38:9728–9740.
Rieke F, Baylor DA (1998) Origin of reproducibility in the responses of retinal rods to single photons. Biophys J 75:1836–1857.

Rivlin-Etzion M, Zhou K, Wei W, Elstrott J, Nguyen PL, Barres BA, Huberman AD, Feller MB (2011) Transgenic mice reveal unexpected diversity of on-off direction-selective retinal ganglion cell subtypes and brain structures involved in motion processing. J Neurosci 31:8760–8769.

Rodieck RW (1998) *The first steps in seeing*. Sunderland, MA: Sinauer Associates.

Sabbah S, Gemmer JA, Bhatia-Lin A, Manoff G, Castro G, Siegel JK, Jeffery N, Berson DM (2017) A retinal code for motion along the gravitational and body axes. Nature 546:492–497.

Sethuramanujam S, McLaughlin AJ, deRosenroll G, Hoggarth A, Schwab DJ, Awatramani GB (2016) A central role for mixed acetylcholine/GABA transmission in direction coding in the retina. Neuron 90:1243–1256.

Sethuramanujam S, Yao X, deRosenroll G, Briggman KL, Field GD, Awatramani GB (2017) "Silent" NMDA synapses enhance motion sensitivity in a mature retinal circuit. Neuron 96:1099–1111.e3.

Shelley J, Dedek K, Schubert T, Feigenspan A, Schultz K, Hombach S, Willecke K, Weiler R (2006) Horizontal cell receptive fields are reduced in connexin57-deficient mice. Eur J Neurosci 23:3176–3186.

Strauss S, Korympidou MM, Ran Y, Franke K, Schubert T, Baden T, Berens P, Euler T, Vlasits AL (2022) Center-surround interactions underlie bipolar cell motion sensitivity in the mouse retina. Nat Commun 13:5574.

Sun LO, Brady CM, Cahill H, Al-Khindi T, Sakuta H, Dhande OS, Noda M, Huberman AD, Nathans J, Kolodkin AL (2015) Functional assembly of accessory optic system circuitry critical for compensatory eye movements. Neuron 86:971–984.

Takeshita D, Smeds L, Ala-Laurila P (2017) Processing of single-photon responses in the mammalian on and off retinal pathways at the sensitivity limit of vision. Philos Trans R Soc Lond B Biol Sci 372:20160073.

Trenholm S, Johnson K, Li X, Smith RG, Awatramani GB (2011) Parallel mechanisms encode direction in the retina. Neuron 71:683–694.

Trenholm S, McLaughlin AJ, Schwab DJ, Awatramani GB (2013) Dynamic tuning of electrical and chemical synaptic transmission in a network of motion coding retinal neurons. J Neurosci 33:14927–14938.

Trenholm S, McLaughlin AJ, Schwab DJ, Turner MH, Smith RG, Rieke F, Awatramani GB (2014) Nonlinear dendritic integration of electrical and chemical synaptic inputs drives fine-scale correlations. Nat Neurosci 17: 1759–1766.

Trong PK, Rieke F (2008) Origin of correlated activity between parasol retinal ganglion cells. Nat Neurosci 11:1343–1351.

Troy JB, Bohnsack DL, Diller LC (1999) Spatial properties of the cat X-cell receptive field as a function of mean light level. Vis Neurosci 16:1089–1104.

Vaney DI (1994) Territorial organization of direction-selective ganglion cells in rabbit retina. J Neurosci 14:6301–6316.

Venkataramani S, Taylor WR (2010) Orientation selectivity in rabbit retinal ganglion cells is mediated by presynaptic inhibition. J Neurosci 30:15664–15676.

Volgyi B, Deans MR, Paul DL, Bloomfield SA (2004) Convergence and segregation of the multiple rod pathways in mammalian retina. J Neurosci 24: 11182–11192.

Volland S, Esteve-Rudd J, Hoo J, Yee C, Williams DS (2015) A comparison of some organizational characteristics of the mouse central retina and the human macula. PLoS One 10:e0125631.

Wang YV, Weick M, Demb JB (2011) Spectral and temporal sensitivity of cone-mediated responses in mouse retinal ganglion cells. J Neurosci 31: 7670–7681.

Wei W (2018) Neural mechanisms of motion processing in the mammalian retina. Annu Rev Vis Sci 4:165–192.

Yao X, Cafaro J, McLaughlin AJ, Postma FR, Paul DL, Awatramani G, Field GD (2018) Gap junctions contribute to differential light adaptation across direction-selective retinal ganglion cells. Neuron 100:216–228.e6.

Yau KW, Matthews G, Baylor DA (1979) Thermal activation of the visual transduction mechanism in retinal rods. Nature 279:806–807.

Yonehara K, Balint K, Noda M, Nagel G, Bamberg E, Roska B (2011) Spatially asymmetric reorganization of inhibition establishes a motion-sensitive circuit. Nature 469:407–410.

Yoshida K, Watanabe D, Ishikane H, Tachibana M, Pastan I, Nakanishi S (2001) A key role of starburst amacrine cells in originating retinal directional selectivity and optokinetic eye movement. Neuron 30:771–780.

Yu WQ, Grzywacz NM, Lee EJ, Field GD (2017) Cell type-specific changes in retinal ganglion cell function induced by rod death and cone reorganization in rats. J Neurophysiol 118:434–454.

Yue WW, Frederiksen R, Ren X, Luo DG, Yamashita T, Shichida Y, Cornwall MC, Yau KW (2017) Spontaneous activation of visual pigments in relation to openness/closedness of chromophore-binding pocket. eLife 6: e18492.

Zhang Y, Kim IJ, Sanes JR, Meister M (2012) The most numerous ganglion cell type of the mouse retina is a selective feature detector. Proc Natl Acad Sci U S A 109:E2391–E2398.

Zhang AJ, Zhang J, Wu SM (2006) Electrical coupling, receptive fields, and relative rod/cone inputs of horizontal cells in the tiger salamander retina. J Comp Neurol 499:422–431.